



The Carousel Lens: A Well-modeled Strong Lens with Multiple Sources Spectroscopically Confirmed by VLT/MUSE

William Sheu¹ , Aleksandar Cikota² , Xiaosheng Huang^{3,4} , Karl Glazebrook^{5,6} , Christopher Storfer^{4,7} , Shrihan Agarwal⁸ , David J. Schlegel⁴ , Nao Suzuki^{4,9,10} , Tania M. Barone^{5,6} , Fuyan Bian¹¹ , Tesla Jeltema¹² , Tucker Jones¹³ , Glenn G. Kacprzak^{5,6} , Jackson H. O'Donnell¹² , and Keerthi Vasan G. C.¹³

¹ Department of Physics & Astronomy, University of California, Los Angeles, 430 Portola Plaza, Los Angeles, CA 90095, USA; wsheu@astro.ucla.edu

² Gemini Observatory/NSF's NOIRLab, Casilla 603, La Serena, Chile

³ Department of Physics & Astronomy, University of San Francisco, 2130 Fulton Street, San Francisco, CA 94117-1080, USA

⁴ Physics Division, Lawrence Berkeley National Laboratory, 1 Cyclotron Road, Berkeley, CA 94720, USA

⁵ Centre for Astrophysics and Supercomputing, Swinburne University of Technology, Hawthorn, Victoria 3122, Australia

⁶ ARC Centre of Excellence for All Sky Astrophysics in 3 Dimensions (ASTRO 3D), Australia

⁷ Institute for Astronomy, University of Hawaii, 2680 Woodlawn Drive, Honolulu, HI 96822-1897, USA

⁸ Department of Astronomy, University of Chicago, 5640 S Ellis Avenue, Chicago, IL 60615, USA

⁹ Department of Physics, Florida State University, 77 Chieftan Way, Tallahassee, FL 32306, USA

¹⁰ Kavli Institute for the Physics and Mathematics of the Universe, University of Tokyo, Kashiwa 277-8583, Japan

¹¹ European Southern Observatory, Alonso de Córdova 3107, Casilla 19001, Vitacura, Santiago 19, Chile

¹² Santa Cruz Institute for Particle Physics, Santa Cruz, CA 95064, USA

¹³ Department of Physics and Astronomy, University of California, Davis, 1 Shields Avenue, Davis, CA 95616, USA

Received 2024 May 18; revised 2024 July 5; accepted 2024 July 18; published 2024 September 11

Abstract

Over the past few years alone, the lensing community has discovered thousands of strong lens candidates, and spectroscopically confirmed hundreds of them. In this time of abundance, it becomes pragmatic to focus our time and resources on the few extraordinary systems, in order to most efficiently study the Universe. In this paper, we present such a system: DESI-090.9854-35.9683, a cluster-scale lens at $z_1 = 0.49$, with seven observed lensed sources around the core, and additional lensed sources further out in the cluster. From the number and the textbook configuration of the lensed images, a tight constraint on the mass potential of the lens is possible. This would allow for detailed analysis on the dark and luminous matter content within galaxy clusters, as well as a probe into dark energy and high-redshift galaxies. We present our spatially resolved kinematic measurements of this system from the Very Large Telescope Multi Unit Spectroscopic Explorer, which confirm five of these source galaxies (in ascending order, at $z_s = 0.962, 0.962, 1.166, 1.432$, and 1.432). With previous Hubble Space Telescope imaging in the F140W and F200LP bands, we also present a simple flux-based lens model consisting of two power-law profiles that, for a cluster lens, well models the five lensed arc families with redshifts. We determine the mass to be $M(< \theta_E) = 4.78 \times 10^{13} M_\odot$ for the primary mass potential. From the model, we extrapolate the redshift of one of the two source galaxies not yet spectroscopically confirmed to be at $z_s = 4.52^{+1.03}_{-0.71}$.

Unified Astronomy Thesaurus concepts: Galaxy clusters (584); Strong gravitational lensing (1643); Galaxy spectroscopy (2171); High-redshift galaxies (734)

1. Introduction

Strong lensing occurs when the gravity of a massive object, typically a galaxy or galaxy cluster, distorts the light path from a background source galaxy with near perfect alignment with the observer. These distortions can result in multiple, magnified, and warped images of the source galaxy surrounding the lensing object. These systems are invaluable probes to many facets of cosmology. By fitting for the lensed images and analyzing the lens galaxy kinematics, we can study the dark matter profiles of the lens (e.g., Shajib et al. 2021). By measuring and modeling the time delays of lensed transient events or variable objects between the multiple images, we can constrain the Hubble constant H_0 , independent of the cosmic microwave background and direct distance ladder measurements, which currently disagree (e.g., Wong et al. 2020). By virtue of its ability to drastically magnify background sources,

strong lensing allows for significantly deeper and further observations than otherwise possible (e.g., Roberts-Borsani et al. 2022).

This paper is organized as follows: we describe the general properties and discovery status of DESI-090.9854-35.9683 (Section 2), provide our analysis of the Multi Unit Spectroscopic Explorer (MUSE) integral field units (IFU) data (Section 3), present our lens model of the system (Section 4), discuss the possible redshift of one of the lensed sources (Section 5), and conclude (Section 6).

2. DESI-090.9854-35.9683 Discovery and Properties

DESI-090.9854-35.9683 (R.A.: $6^{\text{h}}3^{\text{m}}56^{\text{s}}.50$, decl.: $-35^{\circ}58'5''.88$) was first identified in Jacobs et al. (2019) as a “possible, but not probable or definite” strong lens system candidate by applying a convolutional neural network to the Dark Energy Survey (DES) Year 3 imaging. Its low score is likely due to the small cutouts ($26'' \times 26''$) used during visual inspection, which missed the large cluster-scale lensing nature (Jacobs et al. 2019). Huang et al. (2021) later independently identified this system with a residual neural network on the



Original content from this work may be used under the terms of the [Creative Commons Attribution 4.0 licence](https://creativecommons.org/licenses/by/4.0/). Any further distribution of this work must maintain attribution to the author(s) and the title of the work, journal citation and DOI.

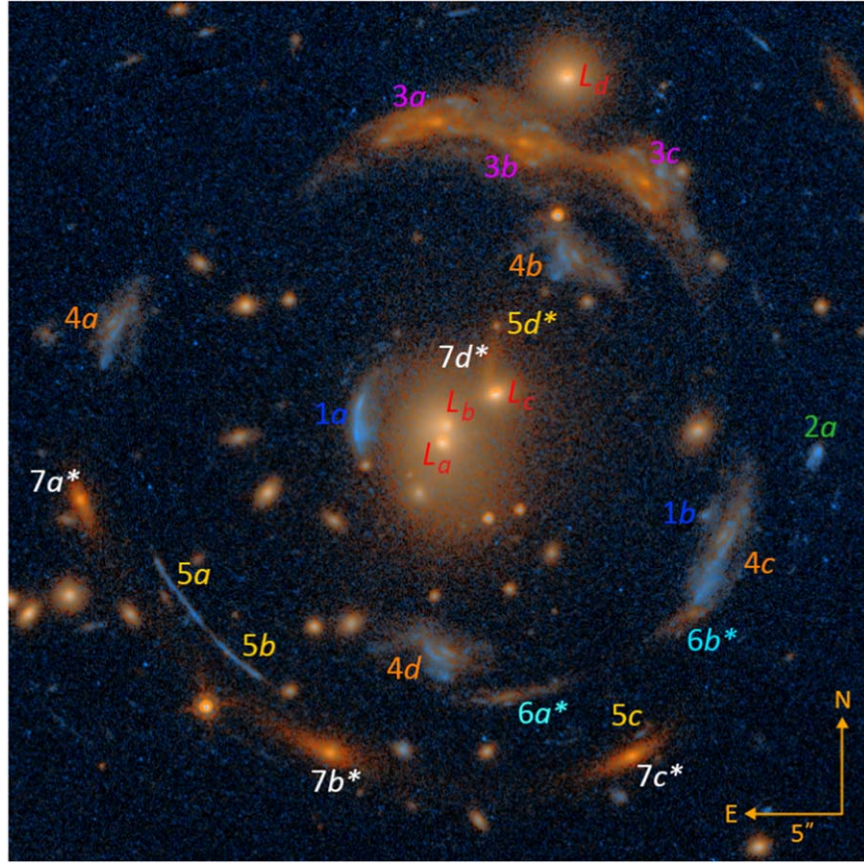


Figure 1. RGB image of DESI-090.9854-35.9683, generated using the HST F140W filter ($0''.070 \text{ pixel}^{-1}$) as the red channel, HST F200LP filter ($0''.028 \text{ pixel}^{-1}$) as the blue channel, and the pixel-wise average of the two filters as the green channel. The brightest cluster-member galaxies within our cutout, labeled as L_a , L_b , L_c , and L_d , are approximately at the same redshift of $z_1 = 0.49$ (see Table 1). The source galaxy images, labeled with a number prefix and a letter, are organized such that images of the same numeral prefix and color correspond to the same source galaxy. Note that $2a$ is the only image for this arc family. Image labels followed by an asterisk indicate that they do not exhibit prominent lines in the MUSE IFU data, and hence we cannot spectroscopically confirm their redshifts. The spectroscopic redshifts of galaxies 1, 2, 3, 4, and 5 are $z_s = 0.962, 0.962, 1.166, 1.432, \text{ and } 1.432$, respectively (see Section 3).

Dark Energy Spectroscopic Instrument (DESI) Legacy Imaging Surveys Data Release 8; following visual human inspection, the system was given a strong lens candidacy grade of A (see their Figure 10). This system was also found by O’Donnell et al. (2022) as DESJ0603-3558, by applying a color-magnitude selection to catalogs created from the first three observing seasons of DES, followed by visual scanning. DESI-090.9854-35.9683 was observed by the Hubble Space Telescope (HST) Wide Field Camera 3 for 600 seconds each in the F140W and F200LP filters (HST proposal #16773; K. Glazebrook), which is shown as an RGB image in Figure 1. All the HST data used in this paper can be obtained from the MAST archive at doi:10.17909/zq07-4f53. Throughout this paper, we will reference the labeling scheme illustrated in Figure 1.

Strong lensing in DESI-090.9854-35.9683 occurs around the center of a small cluster with four spectroscopically confirmed source galaxies, plus one weakly lensed galaxy. While this is a cluster lens, we note that the lens profile does not seem overly complex, as the lensed image configurations for arc families 1, 3, 4, and 7 are typical of simple lens profiles, implying a fairly relaxed lensing potential. Source galaxy 1 ($z_s = 0.962$; see Section 3) is doubly lensed. Source galaxy 2 ($z_s = 0.962$) appears to have only one lensed image, and hence is weakly lensed. The lensed images of source galaxy 3 ($z_s = 1.166$) appear to be in a “naked cusp” configuration (e.g., Bradač et al. 2004), given that there are three bright images merging, and yet

a fourth image is not present in the MUSE data cube nor in our model predictions. Such a configuration is only possible if the lens’s inner diamond caustic extends outside its elliptical caustic, which gives additional insight on the lens potential (e.g., Kochanek 1992; Narayan & Wallington 1992). Also, the source galaxy 3 images are significantly perturbed by one of the cluster-member galaxies L_d , in addition to the main cluster profile centered near galaxies L_a , L_b , and L_c . Source galaxy 4 ($z_s = 1.432$) is quadruply lensed in an Einstein cross configuration; this source exhibits a high level of structural complexity. Source galaxy 5 ($z_s = 1.432$) appears to be quadruply lensed, with a demagnified fourth image $5d$ predicted by our model (see Section 4). Given the similarity in their colors, morphology, and their tangential elongation, we posit that objects $6a$ and $6b$ are lensed images of the same source galaxy, but no spectroscopic redshift can be identified from the MUSE data (though the MUSE data cube does indeed distinguish object $6b$ from $4c$). Source galaxy 7 is quadruply lensed, with $7d$ being a radial arc. Not only is the color of $7d$ consistent with $7a$ – $7c$, but the location is in agreement with lens modeling (see Section 5). There are no prominent spectroscopic lines present for source galaxy 7 in the MUSE observations, but our lens modeling predicts a redshift of $z_s = 4.52^{+1.03}_{-0.71}$ (also in Section 5), which would make it an interesting probe into high-redshift galaxies.

In addition to its prominent lensing features, DESI-090.9854-35.9683 was also identified as a Sunyaev–Zel’dovich galaxy cluster through X-ray detections in the ROSAT All-Sky Survey (Voges et al. 2000; Flesch 2010; Tarrío et al. 2019), and microwave detections from the Atacama Cosmology Telescope (Hilton et al. 2021).

3. MUSE IFU Observations

DESI-090.9854-35.9683 was observed on 2023 September 30, at 07:45 hr UT (Prog. ID 0111.B-0400(H)) with MUSE (Bacon et al. 2010), an IFU spectrograph mounted at UT4 of ESO’s Very Large Telescope (VLT) on Cerro Paranal in Chile. The observations were carried out in the MUSE WFM-NOAO-N mode, with a field of view of $60'' \times 60''$ and a spaxel size of $0''.2$. The spectral range is from 4750 to 9350 Å with the spectral resolution ranging from $R = 2000$ to 4000 Å across the wavelength domain. The observations were taken with 4×700 s exposures during DIMM seeing of $\sim 0''.9$ in clear but windy ($\sim 10 \text{ m s}^{-1}$) weather, and reduced following standard procedures with the MUSE pipeline package version 2.2 (Weilbacher et al. 2020) that is a part of the ESO Recipe Execution Tool (ESOREX). We also removed sky lines using the Zurich Atmosphere Purge sky subtraction tool (Soto et al. 2016).

We extracted the spectra of the lens and the lensed images of the sources from the MUSE data cube and determined the redshifts by matching prominent emission and absorption lines to the spectra (Figure 2). Using the Ca H and K lines, we successfully determine the redshifts of the lensing galaxies ($L_a + L_b$; see Figure 1 for a map of objects), which also display prominent G-band, Mg b, and Na I D absorption lines, and of the lensed images of source galaxies 1, 2, 3, 4, and 5 on account of the [O II] $\lambda\lambda$ 3726.1, 3728.8 doublet. All redshifts are given in Table 1. The lensing galaxies, L_{a+b} , are part of a galaxy cluster. The other two bright members, L_c and L_d , also display prominent absorption lines at a redshift consistent with proper velocities within galaxy clusters. From these three measurements, we calculate a mean cluster redshift of $z = 0.4884 \pm 0.0014$. We also note that the source galaxies 1 and 2 have similar redshifts of $z_s = 0.962$, and source galaxies 4 and 5 have similar redshifts of $z_s = 1.432$. This may indicate that we are observing a series of three galaxy groups/clusters that lie on the same line of sight. Lastly, source galaxy 3 has a redshift of $z_s = 1.166$.

The lensed galaxy 1 displays two arcs, 1a and 1b at consistent redshifts (see Figure 2). Initially, the bright image 2 was thought to be the counterarc of 1a; however, lens modeling (see Section 4) showed inconsistencies with the expected position of the image 1b. Furthermore, the redshift of 2a is also inconsistent with the redshift of 1a (with a 6.3σ discrepancy; see Figure 2 and Table 1). Figure 3 shows a proper velocity difference map of the images, and it is clear that, while all the other images have consistent velocities, the velocity of source 2 is an outlier. A closer inspection of the MUSE cube revealed a faint counterarc, 1b, at the expected position. We conclude that image 2a belongs to a singly lensed galaxy distinct from arc family 1. In image 1a, the [O III] is detected, which could be used to probe the gas-phase metallicity of source galaxy 1 in future analysis.

Source galaxy 3 displays three lensed images north of the lens: 3a, 3b, and 3c, at a redshift of $z_s = 1.166$. In Table 1, we see significant differences in the proper velocity between

images 3a, 3b, and 3c, which we associate as being due to their diffused imaging in the MUSE cube (see Figure 3). Because of this, we cannot well ascertain which part of the source galaxy we are probing through the spectra of each image. Therefore, the significant difference in proper velocities are likely due to rotation/dispersion within the source galaxy, and our spaxel selection capturing different regions of the source galaxy for each image.

The source galaxies 4 and 5 are both quadruply lensed and at a similar redshift of $z_s = 1.432$. The quad lensed images of source galaxy 4 exhibit textbook parities (see right panel of Figure 3), indicating that the central part of the cluster is dynamically relaxed. This, together with the overall relatively high degree of symmetry of this system, motivated a relatively simple lens model in the next section. Although their redshifts are similar, there is a statistically significant difference between source 4 and 5 (of 6.2σ ; see Table 1). Source galaxy 5 displays two bright arcs, clearly visible in the MUSE data (see left panel in Figure 3), 5a and 5b. The position of image 5c is predicted by the lens model and found in the MUSE data cube after closer examination. The image 5c is faint, and so we do not show its spectrum in Figure 2, but the [O II] emission is visible in the line map (see left panel in Figure 3). 5d is also predicted by the lens model, but as it is demagnified and therefore even fainter, it cannot be spectroscopically confirmed by the MUSE data. The images of source galaxy 6 are visible in the near-IR HST images, but very faint in the HST optical F200LP filter, and are not visible in the MUSE (optical) data. The images of source 7 (Figure 6) are faint, but visible in the collapsed MUSE image. However, the extracted spectra do not show any prominent lines, and so we cannot determine the redshift (see more about source galaxy 7 in Section 5).

In the spectra for source galaxies 1–5 (Figure 2), the [O II] doublet is well resolved. Not only does this allow for accurate redshift measurements (as shown in this paper), but it can also be used to probe the densities of these source galaxies. We leave the detailed spectral analysis for future works. Though we do not yet have spectroscopic redshifts for arc families 6 and 7 (6a, b and 7a, b, c, respectively), based on the HST observations (Figure 1), it is clear that they are lensed arcs: (1) by the arrangement of images in these two arc families, namely, they form an arc with the center of curvature matching the center of the cluster; and (2) by the similarity in morphology and color for images 6a and 6b, and for images 7a, b, and c, respectively. More quantitatively for images 7a, b, and c, Table 3 shows that they have very similar spectral energy distributions (SEDs).

4. Lens Modeling

We use LENSTRONOMY,¹⁴ a multipurpose lens modeling software package, to model DESI-090.9854-35.9683, with multiple source redshift planes to account for each source galaxy (Birrer & Amara 2018; Birrer et al. 2021). LENSTRONOMY implements a forward-modeling algorithm to estimate the lens potential and surface brightness profiles, by reconstructing an image of the lensing system and minimizing over the pixel-level residuals with the data. In the Time-Delay Lens Modeling Challenge (TDLMC; Ding et al. 2021), LENSTRONOMY has proved robust and accurate, it was used by multiple

¹⁴ <https://github.com/lenstronomy/lenstronomy>

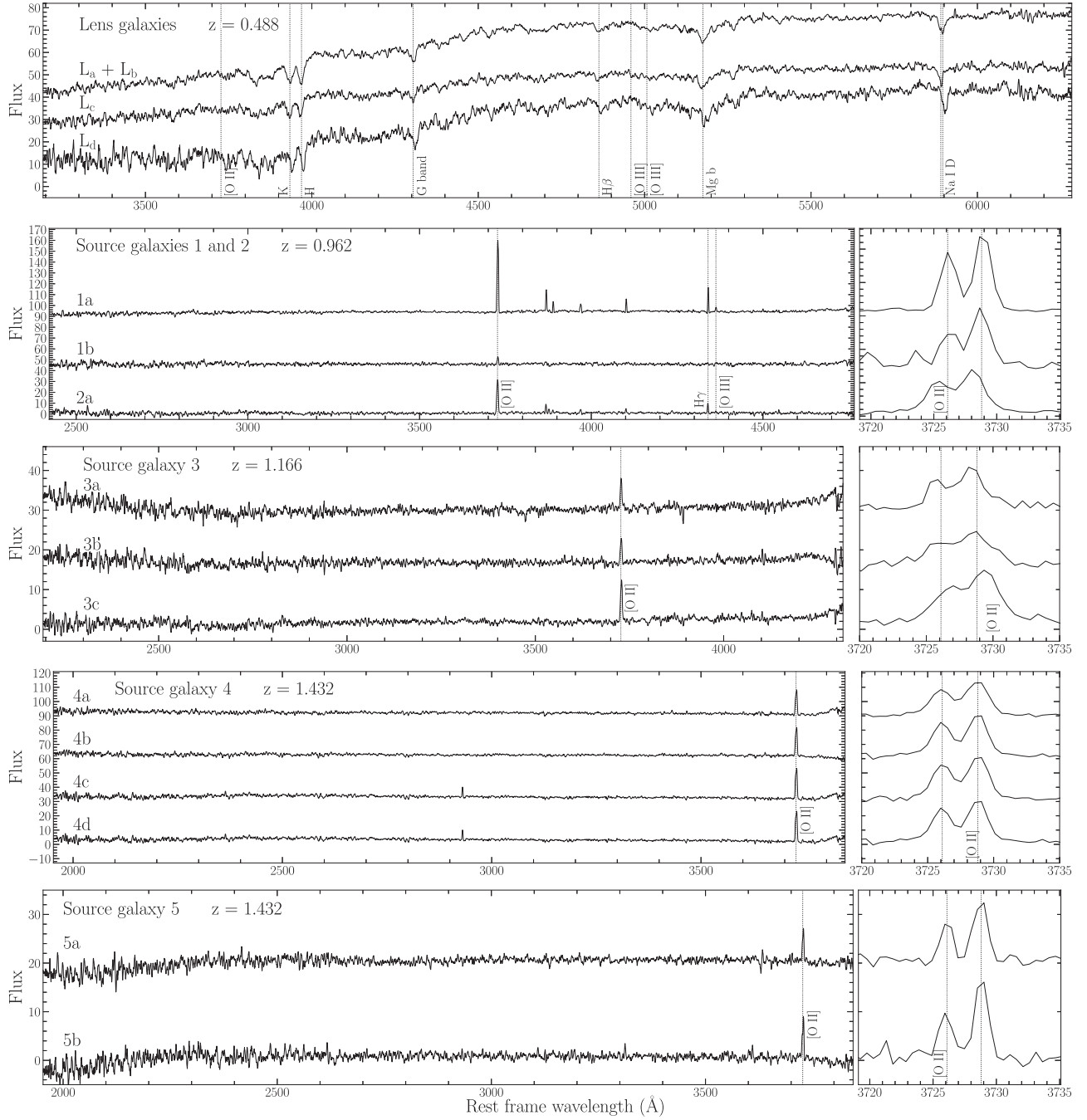


Figure 2. Spectra of the lens and images of the sources extracted from the MUSE cube. The spectra are the average of multiple hand-selected spaxels for each object (see Figure 3). The right panels for the sources are cutouts around the [O II] $\lambda\lambda 3726.1, 3728.8$ doublet line used for the redshift determination.

teams to recover lens model parameters within statistical consistency (in Rung 2).

In this paper, we model based on the F140W image as opposed to the F200LP, as the signal-to-noise ratios (SNRs) in source galaxies 3 and 4 are clearly higher in the F140W filter. Our model consists of two elliptical power-law lens profiles (both at $z_1 = 0.49$), centered at object L_a and L_d respectively. This was the best model (compared to other iterations of power-law lenses centered at L_a , L_b , L_c , and L_d) based on the lowest Bayesian information criterion value using solely lensed image positions. As objects L_a , L_b , L_c , and L_d are the brightest cluster members in the cutout, their light profiles are modeled with elliptical Sérsic profiles (Sérsic 1963) so as to prevent

their lens light from contaminating the lensed images. All other interloping objects, as well as source galaxy 6 and 7 images (since we do not have spectroscopic redshifts for these), are masked out (see the top right panel of Figure 4). The light profiles for source galaxies 1, 3, 4, and 5 are each modeled with an elliptical Sérsic profile and a shapelets basis (Refregier & Bacon 2003; Refregier 2003; Birrer et al. 2015) of order 10, 15, 9, and 8, respectively. These orders are determined through trial and error to improve the model fit with the best reduced χ^2 (e.g., Tan et al. 2024). A Bayesian model comparison is often used to assess and determine how a given model fits the image data (e.g., Nightingale et al. 2018; Shajib et al. 2018), but given the number of sources and the permutations of orders, this

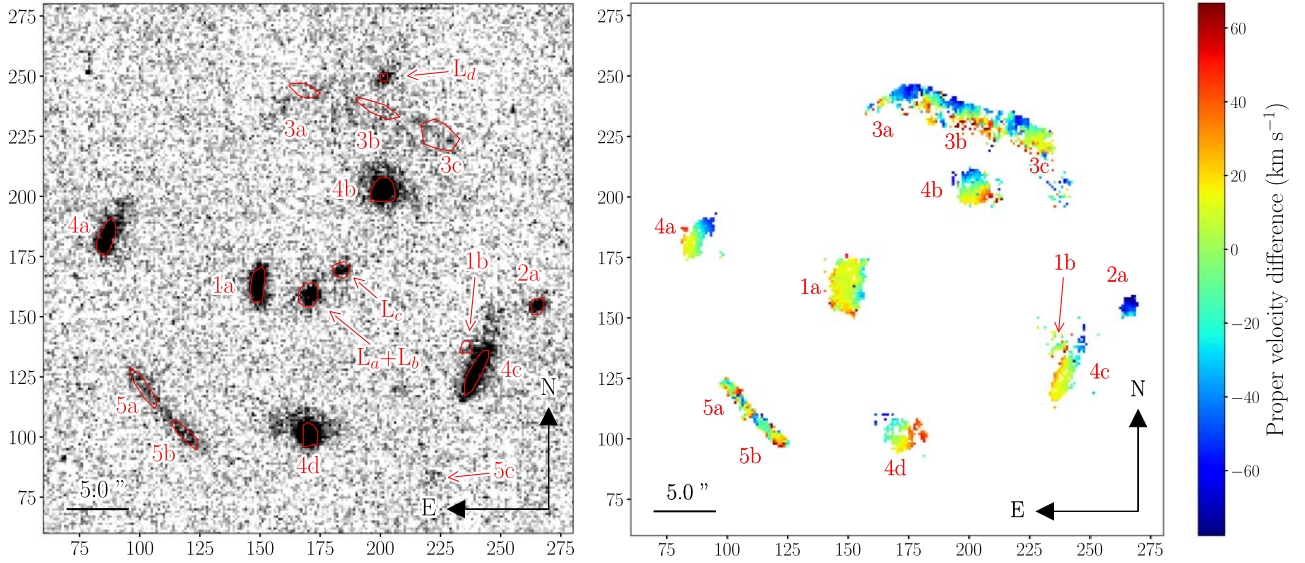


Figure 3. Cutouts of the MUSE data of DESI-090.9854-35.9683. The scale is in pixels, where the pixel size is $0''.2$. North is up, east left. Left: the $[\text{O II}]\lambda\lambda 3726.1, 3728.8$ line map of the images 1, 2, 3, 4, and 5. The red outlines illustrate the spaxels used in generating the spectra in Figure 2. Right: the proper velocity map of the lensed images. The velocity difference is relative to the average redshift for each respective source.

Table 1
Lens and Source Redshifts, and Their Statistical Uncertainties

Object	Redshift	Proper Velocity Difference (km s^{-1})
L_{a+b}	0.48784 ± 0.00045	-123.5 ± 98.8
L_c	0.48716 ± 0.00033	-260.5 ± 77.4
L_d	0.49036 ± 0.00019	384.0 ± 55.1
1a	0.96196 ± 0.00001	25.0 ± 4.2
1b	0.96189 ± 0.00007	14.3 ± 11.4
2a	0.96154 ± 0.00003	-39.2 ± 6.0
3a	1.1657 ± 0.0001	-38.6 ± 17.9
3b	1.1659 ± 0.0002	-19.4 ± 29.9
3c	1.1664 ± 0.0001	58.1 ± 17.8
4a	1.43227 ± 0.00003	-4.9 ± 4.0
4b	1.43230 ± 0.00002	-1.2 ± 2.8
4c	1.43233 ± 0.00002	2.5 ± 2.8
4d	1.43234 ± 0.00002	3.7 ± 2.8
5a	1.43198 ± 0.00004	-1.9 ± 5.8
5b	1.43201 ± 0.00003	1.9 ± 4.8

Note. The redshifts have been determined by fitting the Ca H and K line in the case of the L_{a+b} , L_c and L_d , or the $[\text{O II}]\lambda\lambda 3726.1, 3728.8$ doublet in the case of the lensed images of the sources (1a–5b). The proper velocity difference is calculated as $v_i = c(z_i - z)/(1 + z)$, where z is the average of the images redshifts for each source (or the average of the cluster-member galaxy redshifts in the case of L_{a+b} , L_b , and L_c). The proper velocity for 2a is calculated assuming it is of the same source as 1a and 1b, resulting in the outlying velocity presented.

method would be computationally impractical. For source galaxy 2, we only implement a single elliptical Sérsic profile, as there is only one image present, and its appearance does not necessitate additional complexity. We note that while source 2 (being singly imaged) does not contribute as much constraining power to model as compared to the other lensed sources, the fact that it is singly imaged narrows the lensing parameter

space by forcing the delensed image to lie outside the caustic. While it can be argued that this parameter space is already being excluded by the other image constraints, we nevertheless include source 2 into our model as further confirmation. We model the point-spread function by stacking nearby stars in the HST exposure.¹⁵

We then fit our model to the data, with first a particle swarm optimization operation to locate a maximum (likely close to the global) of the lens likelihood function, then a Markov Chain Monte Carlo algorithm with EMCEE to probe the statistical uncertainties of our model parameters (Foreman-Mackey et al. 2013). The model and its residuals are shown in Figure 4, our parameterizations and statistical uncertainties in Table 2, and the model posteriors are presented in Figure 5. Additionally, we show our model’s predicted lensed image locations over the HST F140W image in Figure 6. We accomplish this by finding the lensed positions of the shapelets source light profile centers for galaxies 1, 3, 4, and 5 (since the shapelets light contribution exhibits a higher peak flux than their Sérsic counterpart); we use the Sérsic profile center for galaxy 2 as we do not model a shapelets profile for it.

The model achieves a reduced χ^2 of 2.3. For the primary lensing power-law profile, we find the best-fit Einstein radius to be $\theta_E = 13''.03 \pm 0.02$ (using $z_s = 1.432$) and the power-law slope, $\gamma = 1.67 \pm 0.01$ (corresponding to a total two-dimensional projected mass within the Einstein radius of $4.78 \times 10^{13} M_\odot$). This is significantly steeper ($\sim 3\sigma$) than population-level total densities of galaxy clusters at $z = 0.2$ – 0.3 (Newman et al. 2013), but could be explained by our model systematics (as discussed in the paragraph after next), and/or galaxy cluster density profile evolution (Mostoghiu et al. 2019).

Through the trial and error of our modeling process, we made several revelations that helped us in identifying the source images. We had initially thought image 2a to be the counterarc of image 1a due to their similar redshifts ($z_s = 0.96196$ for 1a and $z_s = 0.96154$ for 2a; see Table 1),

¹⁵ We apply the implementation provided in <https://github.com/sibirrer/AstroObjectAnalyser>.

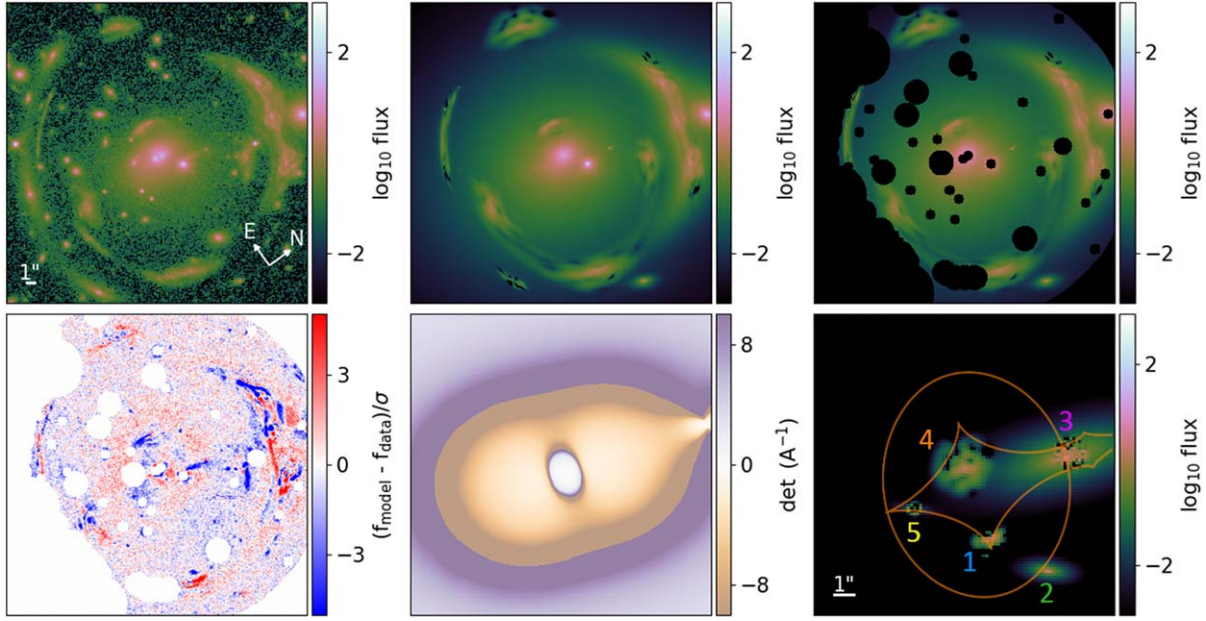


Figure 4. Modeling results for DESI-090.9854-35.9683. Top left: the HST F140W image. Top middle: the resulting best-fitting model. Top right: the best-fitting model, with the masks used in the modeling process. Bottom left: the normalized residuals. Bottom middle: the magnification map at the lens plane assuming $z_s = 1.432$. Bottom right: the source plane image, overlaid with the caustic at $z_s = 1.432$, and labels corresponding to the source galaxies. All panels but the source plane panel (bottom right) share the same compass and scale bar as the data panel (top left).

Table 2
Lens Model Parameters and Their Statistical Uncertainties

Object	θ_E (arcsec)	γ	q	PA (deg)	$M(<\theta_E)$ ($10^{11}M_\odot$)	γ^{ext}	ϕ^{ext} (deg)
L_a	13.03 ± 0.02	1.67 ± 0.01	0.87 ± 0.01	-45 ± 1	478 ± 2
L_d	0.99 ± 0.02	2.12 ± 0.01	0.69 ± 0.01	-38 ± 1	2.77 ± 0.12
External Shear	0.11 ± 0.01	9 ± 1

Note. Here, θ_E is the Einstein radius (with respect to $z_s = 1.432$), γ is the logarithmic slope of the mass profile, q is the mass axis ratio, PA is the mass position angle, $M(<\theta_E)$ is the projected mass within the Einstein radius, γ^{ext} is the external shear magnitude, and ϕ^{ext} is the external shear angle. All angular measures are given as north of east.

relative locations, and similar colors. However, from inconsistencies with our predicted counterarc location, we correctly found image 1b to be the counter image and 2a as a separate lensed galaxy (which is now spectroscopically confirmed; see Table 1). Additionally, through constraining images 5a and 5b, our model placed source galaxy 5 to lie just inside the caustic, predicting two additional images near 5c and 5d (commonly referred to as a “fold” configuration). After reexamining the MUSE data, we confirmed 5c to indeed be a lensed image, though 5d remains to be too dim to resolve its spectra.

Note that the modeling uncertainties presented in this paper are only statistical. For example, our relatively simple model assumes that the primary lens has a uniform γ . From N -body simulation for CDM (e.g., Navarro et al. 1996), the density profile slope of a cluster-scale halo is expected to vary. In this work, we do not account for this possible systematic effect (of a radius-dependent γ) as this would require a significantly more complex model, which we discuss later. Hence we only present the statistical uncertainties associated with our lens model. The best-fit γ we present can be seen as an average logarithmic power-law slope at different Einstein radii (with $z_s = 0.962$, 1.166, and 1.432).

Despite using a relatively simple lens model, we are able to adequately model DESI-090.9854-35.9683. This is likely due

to the fact that DESI-090.9854-35.9683 is relaxed and therefore well approximated as a power law within the Einstein radii regime. However, future high-resolution X-ray, additional high-resolution imaging, and/or deeper spectroscopic observations may warrant increasing the lens model complexity.

5. Inferring the Redshift of Source Galaxy 7

Though we do not have spectroscopic redshift confirmation of source galaxy 7, we can estimate its redshift by extrapolating our lens model. In our model, the only quantities that change with source redshift are the Einstein radii,

$$\theta_E \propto \sqrt{\frac{D_{ls}}{D_s}}, \quad (1)$$

where D_{ls} is the angular diameter distance between the lens and source, and D_s is the angular diameter distance to the source. We can then simply use our best-fit lens model, fix all parameters except the Einstein radii of our two lens potentials (while fixing the ratio between the two), and fit for the source galaxy position that best reproduces the image positions and flux ratios of 7a, 7b, and 7c. From the best-fitting θ_E , we can

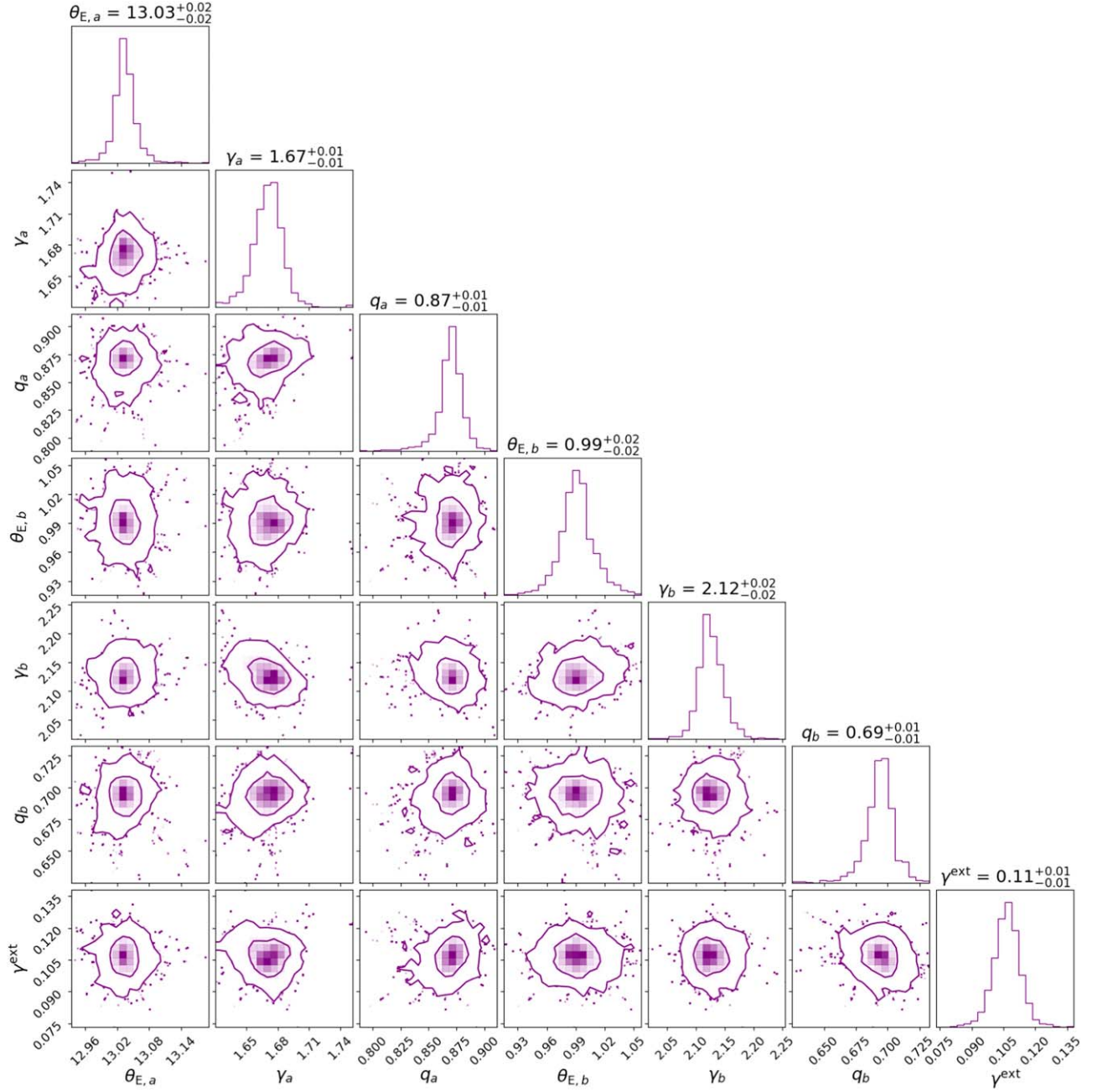


Figure 5. Posteriors of our lens model parameters. Also see Table 2 for a description and summary of each parameter values, as well as the angular configuration components to the lens profiles (i.e., PA_a , PA_b , and ϕ^{ext}). The inner and outer contours in the 2D distributions represent 68th and 95th percentiles, respectively.

estimate the source redshift by assuming a standard flat Λ CDM cosmology of $H_0 = 70 \text{ km s}^{-1} \text{ Mpc}^{-1}$ and $\Omega_M = 0.3$.

The HST F140W observed magnitudes are shown in Table 3. The image locations are assumed to have generous uncertainties of $\pm 0''.5$, to account for possible systematic uncertainty within our model. From these quantities, we fit for the source galaxy position and source redshift that maximizes the log-likelihood of the lensed positions and normalized fluxes of images 7a, 7b, and 7c.

Using this scheme, we estimate source galaxy 7 has a redshift of $z_s = 4.52^{+1.03}_{-0.71}$, and magnifications of $8.56^{+0.20}_{-0.19}$, $12.86^{+0.36}_{-0.34}$, $9.73^{+0.26}_{-0.25}$ at 7a, 7b, and 7c, respectively. While we do not include image 7d in our calculation (since its location and flux are not as well defined as the other images), our best-

fitting results predict a radial arc within $\sim 1''$ of 7d. We reiterate that systematic effects are not accounted for within our models; this estimate assumes a constant γ for the modeled perturbers and the uncertainty is purely statistical (see Section 4). Assuming this redshift, it should be possible to detect Ly α emission within the MUSE data, but we do not detect any prominent lines, possibly due to its absence or the low SNR of source galaxy 7 in the MUSE data.

One possibility is that the Mg II emission line doublet ($\lambda\lambda$ 2796 and 2803; typically prominent in the broad-line region of active galactic nuclei, AGNs) may contribute to the F140W flux at that redshift, and could partially justify its brightness. The general trend in the SED identified from our photometry seem qualitatively similar to the NIRSpec/PRISM spectra of

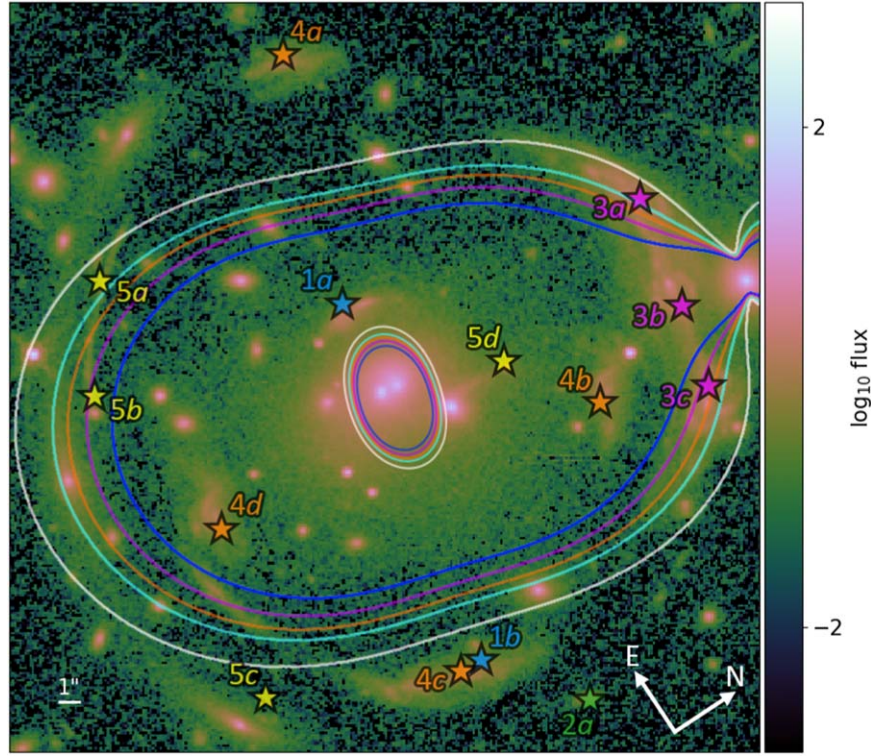


Figure 6. Predicted image locations and critical curves (blue, purple, orange, cyan, and white for $z_s = 0.962, 1.166, 1.432, 1.75,$ and 4.52 , respectively) of our model, plotted over the HST F140W image. We use the centers of the shapelets source light profiles as the source image position on their respective source plane, for source galaxies 1, 3, 4, and 5. We use the Sérsic source light profile center for source galaxy 2, as we do not model for an additional shapelets basis.

Table 3
AB Apparent Magnitudes of Images *7a*, *7b*, and *7c* in Various Bands

Object	DECam <i>g</i> 4730 Å	F200LP 4970 Å	DECam <i>r</i> 6420 Å	DECam <i>i</i> 7840 Å	DECam <i>z</i> 9260 Å	VISTA J 12500 Å	F140W 13920 Å	VISTA Ks 21500 Å
<i>7a</i>	$25.1^{+0.6}_{-0.4}$	$25.5^{+0.4}_{-0.3}$	$23.7^{+0.2}_{-0.1}$	$22.5^{+0.1}_{-0.1}$	$21.9^{+0.1}_{-0.1}$	$23.1^{+0.4}_{-0.3}$	$21.35^{+0.01}_{-0.01}$	$21.5^{+0.5}_{-0.3}$
<i>7b</i>	$25.2^{+0.7}_{-0.4}$	$25.1^{+0.2}_{-0.2}$	$23.1^{+0.1}_{-0.1}$	$22.3^{+0.1}_{-0.1}$	$21.6^{+0.1}_{-0.1}$	$22.2^{+0.1}_{-0.1}$	$21.15^{+0.01}_{-0.01}$	$21.1^{+0.3}_{-0.2}$
<i>7c</i>	$24.8^{+0.4}_{-0.3}$	$25.7^{+0.5}_{-0.5}$	$23.6^{+0.2}_{-0.1}$	$22.6^{+0.1}_{-0.1}$	$21.8^{+0.1}_{-0.1}$	$22.4^{+0.2}_{-0.2}$	$21.24^{+0.01}_{-0.01}$	$21.2^{+0.4}_{-0.3}$
<i>7b</i>	$24.0^{+0.4}_{-0.3}$	$24.8^{+0.6}_{-0.4}$	$22.3^{+0.1}_{-0.1}$	$21.3^{+0.1}_{-0.1}$	$20.7^{+0.1}_{-0.1}$	$21.3^{+0.1}_{-0.1}$	$20.51^{+0.01}_{-0.01}$	$20.3^{+0.2}_{-0.1}$

Note. The first three rows are obtained using a $1''.4$ diameter aperture photometry. The last row uses a larger elliptical aperture photometry ($3.7 \times$ more area) as to capture most of the object's flux; this is only applied onto image *7b* as there are neighboring galaxies near *7a* and *c* that would significantly skew the flux measurements. The band's effective wavelength is given below the band name.

MSAID45924 (Greene et al. 2024), a $z = 4.46$ AGN identified by the James Webb Space Telescope (JWST), though it does not have prominent Mg II emission. However, given we do not observe a point source in any of the images, we find this conclusion unlikely. Another possibility is that this is a high-redshift quiescent galaxy, due to its red color across 5000–21000 Å (see Table 3). HST has identified similar red, quiescent galaxies up to $z = 4$ (e.g., Glazebrook & Schreiber 2017; Schreiber et al. 2018), and JWST up to $z = 5$ (e.g., Carnall et al. 2023; de Graaff et al. 2024; Setton et al. 2024). This theory is supported by the fact that while we faintly observe a continuum for source 7 in the MUSE data, we do not observe any identifiable emission lines, which could indicate quiescence. If this is the case, source galaxy 7 could serve as additional evidence for early galaxy quenching more efficiently than previously understood. With deeper spectroscopy, we will be able to determine the identity and redshift of source galaxy 7 with more confidence.

We do not apply the same analysis on source 6 as we did for source 7 for two reasons. First, we are not certain that the images *6a* and *6b* are indeed of the same source galaxy. Unlike with source 7, where it is visually obvious that *7a*, *b*, and *c* belong to the same source (due to striking similarity in colors and a textbook orientation of its lensed images), this is not the case for source 6. Second, images *6a* and *6b* are much more diffused, complex, and crowded (hence much more difficult to accurately recover photometry for) compared to the compact images of *7a*, *b*, and *c*. As the photometry is a necessary part of the analysis performed on source 7, this would make it much more difficult to accurately estimate a redshift for source 6. Instead, if we assume that images *6a* and *6b* are the same source, we can deduce that the outer critical curve should cross between the two images. From this, our model infers that the redshift of source 6 should lie between $1.75 \leq z_s \leq 4.52$ (see the cyan and white contours of Figure 6).

6. Discussion and Conclusion

In this paper, we present DESI-090.9854-35.9683, a cluster-scale lens first identified in Jacobs et al. (2019), and later independently found in Huang et al. (2021) and O'Donnell et al. (2022). From HST observations in the F140W and F200LP bands (16773; K. Glazebrook), we identify seven possible lensed sources. With spatially resolved spectroscopic observations from MUSE, we confirm five of these lensed sources, and provide the proper velocities for the resolved images. From this, we construct a simple yet successful lens model using only two elliptical power-law mass profiles and external shear. We use this model to infer that one of the spectroscopically unresolved sources (source galaxy 7) is at a redshift of $z_s = 4.52^{+1.03}_{-0.71}$, while the other (source galaxy 6) is at a redshift range of $1.75 \leq z_s \leq 4.52$.

In this spectacular system, nearly all the “classic” lensing configurations are represented. Arc family 2 is singly imaged, as its source is outside of the caustics. The source for arc family 1 is well inside the radial caustic but just outside the tangential (diamond) caustic, and thus is doubly lensed (though there ought to be a third, highly demagnified image near the lens center). Arc family 5 has a predicted fourth image matching an observed object, and forms a “fold” configuration. Whereas arc family 3 has three images, exhibiting a “naked cusp” configuration. Arc family 4 forms a quintessential Einstein cross. Finally, arc family 7 appears to have four images, including a possible radial arc, and if confirmed, this would form a “cusp” configuration (likely also a naked cusp; see Figure 2 of Lewis et al. 2002).

With additional spectroscopic observations to confirm source galaxies 6 and 7, deeper X-ray observations to better constrain the gaseous intracluster medium of this system (e.g., Caminha et al. 2016; Mahler et al. 2023), and/or deeper higher-resolution imaging, we can construct an even more accurate model of this system with fewer assumptions of the total mass profile. In addition to the potential systemic effect of γ varying with cluster-centric radius (see Section 4), another possible systematic effect that a more comprehensive lens model may need to take into account is the gravitational effects of the nearby sources on sources that are further away (i.e., not just multiple source planes, but also multiple lens planes). It then becomes possible to constrain cosmological parameters such as Ω_M and w (e.g., Collett & Auger 2014). Furthermore, the large number of lensed sources can translate to tighter constraints on the matter profile of the lens galaxy, allowing for closer examination of the dark matter and luminous matter distributions/interactions in galaxy clusters.

Clearly, there is much more to be learned from this system. The coincidental alignment of seven galaxies and a foreground galaxy cluster can give us unprecedented insight into the Universe, whether it be high-redshift galaxies, cluster properties, or cosmology.



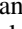

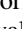
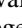









Acknowledgments

This work was supported in part by the Director, Office of Science, Office of High Energy Physics of the US Department of Energy under contract No. DE-AC025CH11231. This research used resources of the National Energy Research Scientific Computing Center (NERSC), a U.S. Department of Energy Office of Science User Facility operated under the same contract as above, and the Computational HEP program in The

Department of Energy’s Science Office of High Energy Physics provided resources through the “Cosmology Data Repository” project (grant No. KA2401022). This research was supported by the Australian Research Council Centre of Excellence for All Sky Astrophysics in 3 Dimensions (ASTRO 3D), through project number CE170100013. The work of A.C. is supported by NOIRLab, which is managed by the Association of Universities for Research in Astronomy (AURA) under a cooperative agreement with the National Science Foundation. X.H. acknowledges the University of San Francisco Faculty Development Fund. T.J. and K.V.G.C. gratefully acknowledge financial support from the National Science Foundation through grant AST-2108515, NASA through grant HST-GO-16773, the Gordon and Betty Moore Foundation through grant GBMF8549, and from a Dean’s Faculty Fellowship. We thank Ned Taylor and Michelle Cluver of the Swinburne University of Technology for providing reduced VISTA 4MOST Hemisphere Survey data.

Software: Lenstronomy (Birrer & Amara 2018; Birrer et al. 2021), NumPy (Harris et al. 2020), SciPy (Virtanen et al. 2020), Matplotlib (Hunter 2007), Astropy (Astropy Collaboration et al. 2013, 2018, 2022), Emcee (Foreman-Mackey et al. 2013), Jupyter (Kluyver et al. 2016), ESO Recipe Execution Tool (Weilbacher et al. 2020), Zurich Atmosphere Purge Sky Extraction Tool (Soto et al. 2016).

ORCID iDs

William Sheu  <https://orcid.org/0000-0003-1889-0227>
 Aleksandar Cikota  <https://orcid.org/0000-0001-7101-9831>
 Xiaosheng Huang  <https://orcid.org/0000-0001-8156-0330>
 Karl Glazebrook  <https://orcid.org/0000-0002-3254-9044>
 Christopher Storfer  <https://orcid.org/0000-0002-0385-0014>
 Shrihan Agarwal  <https://orcid.org/0000-0002-2350-4610>
 David J. Schlegel  <https://orcid.org/0000-0002-5042-5088>
 Nao Suzuki  <https://orcid.org/0000-0001-7266-930X>
 Tania M. Barone  <https://orcid.org/0000-0002-2784-564X>
 Fuyan Bian  <https://orcid.org/0000-0002-1620-0897>
 Tesla Jeltema  <https://orcid.org/0000-0001-6089-0365>
 Tucker Jones  <https://orcid.org/0000-0001-5860-3419>
 Glenn G. Kacprzak  <https://orcid.org/0000-0003-1362-9302>
 Jackson H. O'Donnell  <https://orcid.org/0000-0003-4083-1530>
 Keerthi Vasan G. C.  <https://orcid.org/0000-0002-2645-679X>

References

- Astropy Collaboration, Price-Whelan, A. M., Lim, P. L., et al. 2022, *ApJ*, **935**, 167
- Astropy Collaboration, Price-Whelan, A. M., Sipőcz, B. M., et al. 2018, *AJ*, **156**, 123
- Astropy Collaboration, Robitaille, T. P., Tollerud, E. J., et al. 2013, *A&A*, **558**, A33
- Bacon, R., Accardo, M., Adjali, L., et al. 2010, *Proc. SPIE*, **7735**, 773508
- Birrer, S., & Amara, A. 2018, *PDU*, **22**, 189
- Birrer, S., Amara, A., & Refregier, A. 2015, *ApJ*, **813**, 102
- Birrer, S., Shajib, A., Gilman, D., et al. 2021, *JOSS*, **6**, 3283
- Bradač, M., Schneider, P., Lombardi, M., et al. 2004, *A&A*, **423**, 797
- Caminha, G. B., Grillo, C., Rosati, P., et al. 2016, *A&A*, **587**, A80
- Carnall, A. C., McLure, R. J., Dunlop, J. S., et al. 2023, *Natur*, **619**, 716
- Collett, T. E., & Auger, M. W. 2014, *MNRAS*, **443**, 969
- de Graaff, A., Setton, D. J., Brammer, G., et al. 2024, arXiv:2404.05683
- Ding, X., Treu, T., Birrer, S., et al. 2021, *MNRAS*, **503**, 1096
- Flesch, E. 2010, *PASA*, **27**, 283
- Foreman-Mackey, D., Hogg, D. W., Lang, D., & Goodman, J. 2013, *PASP*, **125**, 306

- Glazebrook, K., Schreiber, C., Labbé, I., et al. 2017, *Natur*, **544**, 71
- Greene, J. E., Labbe, I., Goulding, A. D., et al. 2024, *ApJ*, **964**, 39
- Harris, C. R., Millman, K. J., van der Walt, S. J., et al. 2020, *Natur*, **585**, 357
- Hilton, M., Sifón, C., Naess, S., et al. 2021, *ApJS*, **253**, 3
- Huang, X., Storfer, C., Gu, A., et al. 2021, *ApJ*, **909**, 27
- Hunter, J. D. 2007, *CSE*, **9**, 90
- Jacobs, C., Collett, T., Glazebrook, K., et al. 2019, *ApJS*, **243**, 17
- Kluyver, T., Ragan-Kelley, B., Pérez, F., et al. 2016, in *Positioning and Power in Academic Publishing: Players, Agents and Agendas*, ed. F. Loizides & B. Schmidt (Amsterdam: IOS Press), 87
- Kochanek, C. S. 1992, *ApJ*, **384**, 1
- Lewis, G. F., Carilli, C., Papadopoulos, P., & Ivison, R. J. 2002, *MNRAS*, **330**, L15
- Mahler, G., Jauzac, M., Richard, J., et al. 2023, *ApJ*, **945**, 49
- Mostoghiu, R., Knebe, A., Cui, W., et al. 2019, *MNRAS*, **483**, 3390
- Narayan, R., & Wallington, S. 1992, in *Gravitational Lenses*, ed. R. Kayser, T. Schramm, & L. Nieser (Berlin: Springer), 12
- Navarro, J. F., Frenk, C. S., & White, S. D. M. 1996, *ApJ*, **462**, 563
- Newman, A. B., Treu, T., Ellis, R. S., et al. 2013, *ApJ*, **765**, 24
- Nightingale, J. W., Dye, S., & Massey, R. J. 2018, *MNRAS*, **478**, 4738
- O'Donnell, J. H., Wilkinson, R. D., Diehl, H. T., et al. 2022, *ApJS*, **259**, 27
- Refregier, A. 2003, *MNRAS*, **338**, 35
- Refregier, A., & Bacon, D. 2003, *MNRAS*, **338**, 48
- Roberts-Borsani, G., Morishita, T., Treu, T., et al. 2022, *ApJL*, **938**, L13
- Schreiber, C., Labbé, I., Glazebrook, K., et al. 2018, *A&A*, **611**, A22
- Sérsic, J. L. 1963, *BAAA*, **6**, 41
- Setton, D. J., Khullar, G., Miller, T. B., et al. 2024, arXiv:2402.05664
- Shajib, A. J., Birrer, S., Treu, T., et al. 2018, *MNRAS*, **483**, 5649
- Shajib, A. J., Treu, T., Birrer, S., & Sonnenfeld, A. 2021, *MNRAS*, **503**, 2380
- Soto, K. T., Lilly, S. J., Bacon, R., Richard, J., & Conseil, S. 2016, *MNRAS*, **458**, 3210
- Tan, C. Y., Shajib, A. J., Birrer, S., et al. 2024, *MNRAS*, **530**, 1474
- Tarrío, P., Melin, J.-B., & Arnaud, M. 2019, *A&A*, **626**, A7
- Virtanen, P., Gommers, R., Oliphant, T. E., et al. 2020, *NatMe*, **17**, 261
- Voges, W., Aschenbach, B., Boller, T., et al. 2000, *VizieR On-line Data Catalog*, **9029**
- Weilbacher, P. M., Palsa, R., Streicher, O., et al. 2020, *A&A*, **641**, A28
- Wong, K. C., Suyu, S. H., Chen, G. C. F., et al. 2020, *MNRAS*, **498**, 1420